

# Open Research Online

---

The Open University's repository of research publications and other research outputs

## Simulated annealing approach to vascular structure with application to the coronary arteries

### Journal Item

#### How to cite:

Keelan, Jonathan; Chung, Emma M. L. and Hague, James P. (2016). Simulated annealing approach to vascular structure with application to the coronary arteries. Royal Society Open Science, 3(2) pp. 150431–150445.

For guidance on citations see [FAQs](#).

© 2016 The Authors



<https://creativecommons.org/licenses/by-nc-nd/4.0/>

Version: Version of Record

Link(s) to article on publisher's website:

<http://dx.doi.org/doi:10.1098/rsos.150431>

<http://dx.doi.org/10.1098/rsos.150431>

---

Copyright and Moral Rights for the articles on this site are retained by the individual authors and/or other copyright owners. For more information on Open Research Online's data [policy](#) on reuse of materials please consult the policies page.

---

[oro.open.ac.uk](http://oro.open.ac.uk)



**Cite this article:** Keelan J, Chung EML, Hague JP. 2016 Simulated annealing approach to vascular structure with application to the coronary arteries. *R. Soc. open sci.* **3**: 150431. <http://dx.doi.org/10.1098/rsos.150431>

Received: 28 October 2015

Accepted: 15 January 2016

**Subject Category:**

Structural biology and biophysics

**Subject Areas:**

computational biology/biophysics/  
theoretical biology

**Keywords:**

vascular modelling, optimization,  
cardiovascular systems, simulated annealing

**Author for correspondence:**

James P. Hague

e-mail: [jim.hague@open.ac.uk](mailto:jim.hague@open.ac.uk)

Electronic supplementary material is available at <http://dx.doi.org/10.1098/rsos.150431> or via <http://rsos.royalsocietypublishing.org>.

# Simulated annealing approach to vascular structure with application to the coronary arteries

Jonathan Keelan<sup>1</sup>, Emma M. L. Chung<sup>2</sup> and James P. Hague<sup>1</sup>

<sup>1</sup>Department of Physical Sciences, The Open University, Milton Keynes MK7 6AA, UK

<sup>2</sup>Department of Cardiovascular Sciences, University of Leicester, Leicester LE1 5WW, UK

Do the complex processes of angiogenesis during organism development ultimately lead to a near optimal coronary vasculature in the organs of adult mammals? We examine this hypothesis using a powerful and universal method, built on physical and physiological principles, for the determination of globally energetically optimal arterial trees. The method is based on simulated annealing, and can be used to examine arteries in hollow organs with arbitrary tissue geometries. We demonstrate that the approach can generate *in silico* vasculatures which closely match porcine anatomical data for the coronary arteries on all length scales, and that the optimized arterial trees improve systematically as computational time increases. The method presented here is general, and could in principle be used to examine the arteries of other organs. Potential applications include improvement of medical imaging analysis and the design of vascular trees for artificial organs.

## 1. Introduction

Arterial trees are vital for the efficient transport of oxygen and nutrients to tissue. Their anatomy has been studied for many centuries through the dissection of cadavers, inspection of corrosion casts, medical imaging techniques and computational models. It has been determined that individual arterial bifurcations follow optimality principles that lower metabolic demand locally [1–6], as demonstrated by the scaling laws followed by arterial trees [7–11]. More recently, there has been a high level of interest in models that mimic arterial growth (angiogenesis) using physical and physiological principles to simulate vascular anatomy. These models are created based on local optimization principles, where the anatomy of each branch in the arterial tree is governed by a compromise between maximizing fluid

dynamical efficiency and minimizing the quantity of blood required. However, models of coronary vasculature, based on local optimization are not able to explain if the organization of major arteries is the result of fluid dynamical optimization across the ‘whole organ’ [12–16].

The relationship between the radii of vessels in individual bifurcations is well categorized by the equation:  $r_p^\gamma = r_{d_1}^\gamma + r_{d_2}^\gamma$ , where  $r_p$  is the radius of the parent artery,  $r_{d_{1,2}}$  those of the daughter arteries and  $\gamma$  is the bifurcation exponent [4,17,18], which has the value 3.0 in Murray’s formulation. This relation arises from the combination of the continuity equation and the diameter–flow rate relation [9]. Several current methods for *in silico* growth of vascular trees into a simulated tissue substrate aim to optimize the local properties of individual bifurcations [15,19]. A procedure, known as constrained constructive optimization (CCO), starts by inserting a single artery into the tissue. A new vessel with a position chosen at random is then connected to the original artery and the link point is moved such that the energy of the arteries is minimized. New arteries are then iteratively added and optimized until a predetermined number of terminal sites have been added. The overall result is that CCO and similar methods create trees whose structure is predetermined by the order in which new arteries are added: if the order is changed, the final tree structure also changes. Morphologically, CCO reproduces a reasonable distribution of vessel sizes due to the application of Murray’s law, but creates arterial branches that are more symmetric than those found in nature (especially for the largest arteries) [20] and significant extensions are required to generate vessels in hollow organs [21]. The variations in the structure and positions of larger arteries in CCO generated trees are problematic, as organs such as the heart exhibit only small differences in large artery structure over a population (aside from rare abnormalities). An alternative method known as global constructive optimization (GCO) attempts to overcome the problems of CCO by including a multiscale pruning update that is global in the sense that it acts simultaneously on a significant subset of the tree, but otherwise only includes updates allowing local modifications to the topology of the tree. As such, GCO is limited to sampling a subset of the allowed topologies of the arterial trees [22], so while it is expected to offer improvements over CCO, it carries no guarantee of reaching the global minimum. Due to the use of local downhill searches, GCO also has similar issues with hollow organs. To obtain a universal optimization technique to compute *in silico* arterial trees for arbitrary tissue structures, a different approach is needed.

Another method for the generation of large scale arterial trees uses extensive morphological databases [14,23]. These trees contain far more vessels than is feasible to generate with techniques such as CCO, as the topology of the tree is taken from experimental data. However, as detailed morphological databases do not exist for the vast majority of organs, the use of these techniques is impossible in the general case. Morphologically generated models provide trees suitable for large scale fluid dynamical studies and organ phantoms [24]. They achieve this by reproducing experimental data in a computationally accessible form. As such they have no predictive powers that can contribute to the understanding of the origins of arterial tree structure.

A separate class of models exist for use in modelling the growth of tumourous vasculature and the process of vascular remodelling, which involve the direct simulation of sprouting angiogenesis [25–28]. These models seek to reproduce the rapid and dynamic process of tumour vascularization, or the growth of vasculature in normal tissue as it grows. Using *in silico* simulation of sprouting angiogenesis to obtain the vascular structure in a fully grown organ would be extremely difficult, as full details of the distribution of tissue and oxygen demands would be needed for all stages of embryonic and childhood development. As organs such as the heart have very small levels of variation in vascular structure over the population, the structure itself is likely to be caused by a process different from that of tumour vascularization. We suggest that this process is an optimum seeking one, and that as such an optimization procedure is required to accurately model it. We examine if, regardless of the complex processes that guide angiogenesis during growth, the final structure of the coronary vasculature in adult mammals is near optimal.

Development of a method which reaches a morphologically accurate solution based solely upon optimization criteria would be useful in vascular research, allowing for the modelling of realistic vascular trees in organs lacking extensive morphological databases. The inability of CCO and extensions to find the global energy minimum, and the subsequent lack of consistent structure (particularly of the larger arteries), is problematic if organ specific vasculature is required. An approach capable of producing an arterial tree, which minimizes pumping power and blood volume, while providing adequate blood flow to critical regions would be invaluable in this regard. This paper goes beyond previous work by introducing a far more flexible and universal method for generation of ‘whole organ’ arterial trees, in any arbitrarily shaped tissue substrate, that obeys both local and global optimization criteria. To identify globally optimized arterial trees, we use a powerful computational technique known as simulated

annealing (SA) [29]. Although SA is computationally expensive, correctly applied SA techniques have a key advantage of being mathematically and computationally proved to converge to a global energy minimum. To achieve this, our SA-based approach has the potential to sample all possible arterial tree configurations, ranging from perfectly symmetric, intricately bifurcating structures, to asymmetric trees characterized by a single trunk vessel. This is achieved by allowing: (i) repositioning of bifurcations and (ii) swapping the parent vessels of bifurcations between different parts of the tree. By introducing these forms of plasticity to our models, the entire parameter space of the tree can be explored, allowing the method to identify the best possible arterial configuration for supplying a particular organ. Full details of this novel method can be found at the end of the article. As an example application we determine the near optimal configuration of arteries for supplying the heart and compare our computer generated coronary vasculature with morphological data from real coronary arteries. Specifically, we determine that the observed anatomy of the coronary arteries is similar to that expected from near global minimization of total energy expenditure, and validate the approach against porcine data, finding a very high level of agreement with morphological data.

## 2. Methods

The main purpose of any arterial tree is to maintain adequate blood perfusion with minimal total metabolic expense. The suitability of an arterial tree for this purpose is governed by two considerations: (i) as blood is viscous, the power required to pump blood through the vasculature should be minimized and (ii) as energy is required to generate and maintain blood, the volume of blood required should be minimized. Murray's law achieves this for individual bifurcations, but the optimal organization of large numbers of connected bifurcations is far from obvious. The interplay between these competing concerns for thousands of arterial segments leads to a complex optimization problem. Note that in the following, bifurcations will be referred to as nodes, arteries will be referred to as 'segments between nodes', and terminal arterioles are referred to as 'end nodes'.

### 2.1. Metabolic cost to maintain blood volume

The first component of the approach involves calculating the power needed to maintain the entire tree, which will be used as a value in the cost function. The power consumption of the tree can be split into two separate parts: the first is the metabolic cost of maintaining the blood volume and tissue associated with the tree, and the second is the power required to pump blood through the tree. The length and radius of each segment (vessel)  $i$  of the tree must be known to calculate the volume. By assuming a fixed bifurcation exponent, the radii are determined by the topology and only vessel lengths rely on the geometrical arrangement. To calculate the cost, volume must be multiplied by a constant,  $m_b$ , corresponding to a physiologically reasonable metabolic demand of the same quantity of blood and vascular tissue [30]. Thus, the metabolic cost due to the volume of the tree will be given by

$$C_v = m_b V_{\text{tree}}, \quad (2.1)$$

where  $m_b$  is taken to be  $641.3 \text{ J s}^{-1} \text{ m}^{-3}$  and  $V_{\text{tree}}$  is the volume of the entire tree.

### 2.2. Power cost to pump blood through vessels

To calculate the power needed to pump blood through the entire tree, we must know the pressure and volumetric flows inside each segment (vessel) of the tree, which can be found by first assuming that Poiseuille's law,  $\Delta p = QR$ , is followed inside the segments, where  $\Delta p$  is the pressure drop over the vessel, and  $Q$  is the flow. The assumption that flow is laminar inside the vessels is justified provided that the typical length of a vessel is much larger than the radius, and that pulsatile flow effects are negligible. Vessels within the simulated trees have a typical length radius ratio of 10, and while in the largest arteries of the tree pulsatile effects may still be present, these rapidly decay so that the vast majority lie within a non-pulsatile regime. We assume both Murray's law and that terminal node flows are constant to simplify calculation of the relevant fluid dynamical quantities: the only quantity which relies on the structure of the tree is the pressure. In a sense, the segments can be considered as connected set of resistors, with the resistance given by

$$R = \frac{8\mu L}{\pi r^4}, \quad (2.2)$$

where  $r$  is the radius of the vessel,  $L$  its length and  $\mu = 3.6 \times 10^{-3}$  Pa s the viscosity of blood. The pressures (and hence flows) for every node in the tree can then be found recursively.  $W_i$ , the power consumed by each segment  $i$ , is then calculated using

$$W_i = Q_i^2 R_i. \quad (2.3)$$

Summing over all segments in the tree, the total power required to maintain the proper flow through the tree is

$$C_w = \sum_i^{N_{\text{tot}}} W_i. \quad (2.4)$$

### 2.3. Ensuring tissue supply

The primary purpose of the vascular tree is to supply blood; thus it is important that terminal nodes are correctly dispersed inside the tissue. Initially, terminal nodes are randomly distributed inside the tissue, with each node having associated with it a sphere of influence for blood supply. The radius of this sphere is calculated using physiological values for the blood demand of the tissue. The density of myocardium is  $\rho = 1.06 \times 10^3 \text{ kg m}^{-3}$  [31], and the flow demand is  $1.13 \text{ ml min}^{-1} \text{ g}^{-1}$  [32] leading to a flow demand per cubic metre of heart tissue of  $q_{\text{required}} = 2 \times 10^{-2} \text{ s}^{-1}$ . The total flow into the heart is  $Q_0 = 4.16 \times 10^{-6} \text{ m}^3 \text{ s}^{-1}$  [33], which can be converted to total flow per node as  $Q_N = Q_0/N$ , where  $N$  is the total number of arterioles (end nodes). The radius of the supply sphere is then calculated via  $4\pi R_{\text{supply}}^3/3 = Q_N/q_{\text{required}}$ . The sphere can be thought of as a microcirculatory ‘black box’ [15], where the exact fluid dynamical details of the blood flow have been ignored. Spheres of blood supply associated with end nodes are stored in a voxel map (a voxel is a three-dimensional generalization of a pixel) of the tissue, where each terminal node adds exactly one to each voxel inside its sphere of supply (figure 1*b*). While blood demand is not constant within the myocardium at any single instance of time, the majority of fluctuations are high frequency oscillations which are assumed to be averaged out in the present model [34]. The terminal nodes are then allowed to move inside the tissue, where after each move a new voxel supply map is calculated, and the overlap (each voxel supplied by more than one sphere, or the dark red voxels in figure 1*b*) is used as a value in the cost function of the SA algorithm. In addition, all voxels not being supplied are given a cost, so that the overall penalty associated with having both unsupplied and oversupplied voxels is chosen to be

$$C_s = \sum_{\text{voxels}} s; \quad s = \begin{cases} 10 & \text{if } b = 0 \\ (b - 1)^2 & \text{otherwise,} \end{cases} \quad (2.5)$$

where  $b$  is the value of the supply at the voxel and the sum is performed over all the voxels comprising the tissue. In practice, this cost is set to be much larger than all other costs, as any unsupplied tissue would die. Therefore, the terminal nodes spread evenly through the tissue early in the optimization. Other functions may be used, provided that the minimum in the function for each voxel occurs at  $b = 1$ . The value  $C_s$  then defines the fitness of the tree to supply blood, and the penalty for over supplying voxels forms a sort of self-avoidance algorithm, where terminal nodes are encouraged to pack the tissue as densely as possible without overlapping. A benefit of this method is that it allows easy integration of medical imaging into the model, as well as providing an easy method for differentiating tissue with different blood supply demands.

### 2.4. Exclusion of large vessels from tissue

In order to create a realistic vascular tree, it must be possible to exclude some segments from penetrating the tissue. For instance, in the case of the heart, it would be unlikely to find a very large artery within the myocardium, and vessels may not penetrate the ventricles; rather, the larger arteries and arterioles lie on the surface of the heart, with only the smaller arterioles and capillaries being found inside the tissue. To mimic this structure, the approach makes use of a cut-off radius  $R_{\text{cutoff}}$ , whereby segments with radius larger than  $R_{\text{cutoff}}$  may not penetrate the tissue. In the calculations performed in this article,  $R_{\text{cutoff}} = 0.01 \text{ mm}$ . To determine which segments with radius greater than  $R_{\text{cutoff}}$  have penetrated the tissue we first take a distance transform of the tissue surface for each tissue voxel (figure 1*a*). This provides a second voxel map of the tissue, distinct from the blood supply map, giving a measure of the distance of a point from the surface when it is inside the tissue (outside of the surface, the value is zero). For each segment satisfying the radius criteria, a list of voxels that its centre-line penetrates is generated [35], along with

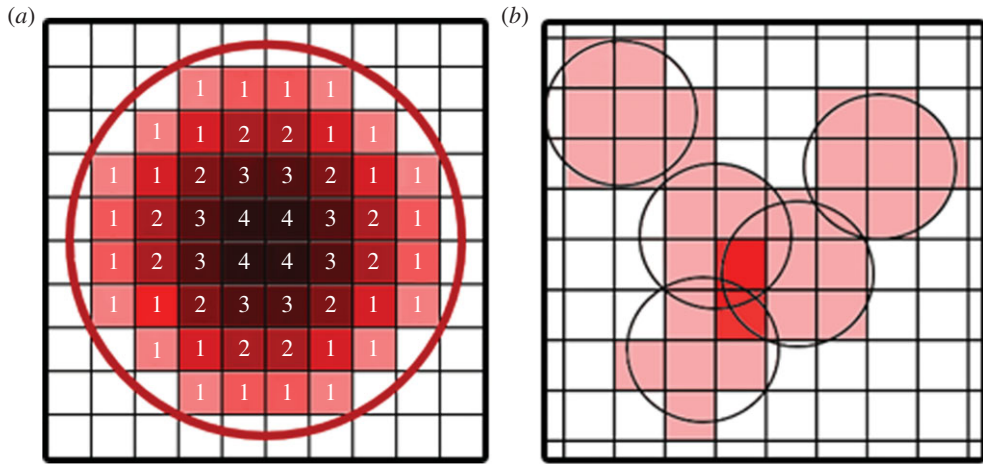


**Figure 1.** (a) The distance map for a spherical surface. Voxels outside the surface have value 0, with those inside the surface contributing a value relating to their distance from the surface. (b) Each arteriole supplies a spherical region shown by the lightly shaded squares. Where there is significant overlap between two spheres, there is a penalty. Unsupplied voxels also incur a penalty in the cost function.

a value for the length element of the segment present inside that voxel. A cost is then calculated based upon the value of the distance transform at each of the voxels according to

$$C_o = \pi r^2 (D_{ijk} \tilde{L}_{ijk})^6, \quad (2.6)$$

where  $i, j$  and  $k$  are the Cartesian voxel coordinates taken from the centre-line of the segment.  $D_{ijk}$  is the value of the distance transform at that voxel coordinate.  $\tilde{L}_{ijk}$  is the length of the segment spent inside the voxel. The sum is performed over all the voxels contained in the list calculated from the centre-line. This cost can then be used in the SA algorithm as a penalty that favours moving large segments out of the tissue.

## 2.5. Pressure constraints

In physiologically realistic trees, capillary networks should receive a constant pressure  $P_{\text{term}}$  to function correctly. A new cost can be devised to ensure this. A suitable candidate is

$$C_p = \sum_i^{N_{\text{term}}} (P_i - P_{\text{term}})^2, \quad (2.7)$$

where the sum is performed over all terminal nodes, and  $P_i$  is the actual terminal node pressure. In practice, for trees which can be optimized on feasible time scales (i.e. of a few thousand nodes), the pressure drop from root to end node is less than 1% of the total pressure drop of a real arterial tree, with most of the pressure drop occurring over smaller arterioles than those considered here, so it is unnecessary to perform this calculation. When it becomes possible to grow larger trees, the pressure at the capillaries will need to be taken into consideration. This will add a significant computational cost.

## 2.6. Total cost function

We have now determined a form for all the relevant costs associated with an arbitrary tree configuration supplying arbitrary tissue shapes. We can therefore define a total cost which gives a numeric measure of the fitness of a given tree,

$$C_T = A_{w,v}(C_w + C_v) + A_o C_o + A_p C_p + A_s C_s, \quad (2.8)$$

where  $A_i$  indicates a weighting value which scales each relevant cost. There is no way to analytically determine what weights to use, and the selection of appropriate weights must be found experimentally; however, a few basic principles such as having a very high weight for the blood supply cost and a low weight for the end node pressure cost can guide the process. In principle,  $A_s$  should be infinite, as tissue without supply dies. In this work, we use  $A_{w,v} = 1 \times 10^4$ ,  $A_p = 0$ ,  $A_s = 1 \times 10^{30}$  and  $A_o = 100$ . In this way,  $A_s$  and  $A_o$  force the exclusion of vessels and uniform supply of tissue to act like constraints. While the



exclusion cost should technically be infinite, as no arteries are found in the ventricles of living humans, it is advantageous to give it a large but finite value. This allows the optimization procedure to identify gradients, giving it extra information and speeding up convergence. This size of the constant for  $A_o$  may seem small in this regard; however, its value  $C_o$  is already raised to the power 6 in equation (2.6). As any scaling of the cost function does not effect the location of minima, we can absorb one of the weightings by scaling everything else. This allows a new cost function  $\bar{C}_T = C_T/A_{w,v}$  to be defined.

## 2.7. Simulated annealing

To select the fittest, most optimized trees, we use a powerful technique for optimization problems known as SA [36,37]. The primary difference between SA and a conventional downhill search is that SA also spends some time exploring solutions with higher cost function, and in this way can climb out of shallow valleys in the fitness function to explore other deeper regions.

The total cost  $C_T$  will play the role of energy in the SA algorithm, so that the probability of accepting a change to a tree of cost  $C_T^i$ , resulting in a tree of cost  $C_T^f$  is given as

$$P_i^f = \begin{cases} \exp\left(-\frac{\Delta C_T}{T}\right) & \text{if } \Delta C_T > 0 \\ 1 & \text{otherwise,} \end{cases} \quad (2.9)$$

where  $P_i^f$  is the probability of going from state  $i$  to state  $f$ ,  $\Delta C_T = C_T^f - C_T^i$  is the change in the cost function associated with going from state  $i$  to  $f$ , and  $T$  is the SA temperature parameter (not be confused with ambient temperature). The small probability to accept a higher cost tree during update allows the tree to climb out of local valleys in the cost function. The algorithm proceeds by making changes to the tree structure, calculating the change in cost function, and then either accepting or rejecting the change by comparing  $P_i^f$  with a random number between 0 and 1.  $T$  starts large and is reduced slowly. If  $T$  has been reduced sufficiently slowly, then the global minimum of the cost function is guaranteed to be reached. In practice, the problem space is too large to achieve this in reasonable time, and slightly different trees with very similar cost are found if the algorithm is run with several random number seeds. The most important consideration is the lowest achieved cost. As such, if the structure of trees generated varies between different runs, we always display data from the run with the lowest cost function. As computational power increases, longer runs will be achievable leading to progressively better optimizations. The highest  $T$  used here is  $1 \times 10^{10}$ , dropping during the algorithm to  $10^{-5}$ . Typically, a tree containing 1000 nodes will need  $10^9$  updates, with a doubling of nodes taking roughly quadruple the number of updates (up to approx. 6000 nodes with one month of CPU time). The large value of  $A_s$  means that the supply of tissue is determined by downhill search, while all other costs are minimized by SA.

## 2.8. Exploring the tree structure: translations and node swaps

The SA algorithm must have access to set of updates which allow it to alter the configuration of the tree. It is necessary to find changes that can be made to the topological and geometrical structure of the tree such that all possible solutions between perfectly symmetric structures and a single trunk vessel can be explored (i.e. the algorithm is ergodic). This is achieved by allowing: (i) repositioning of bifurcations, which is achieved by translating a node in space (figure 2a) and (ii) swapping the parent vessels of bifurcations between different parts of the tree (figure 2b). For all nodes but the root node, this move is valid, and performed consecutively it allows all possible tree topologies to be explored. If one of the two nodes is a direct parent of the other (i.e. while traversing up the tree from one of the chosen nodes, the other node is encountered) the move is rejected to avoid forming a closed loop. With these two updates, the entire parameter space of the tree can be explored, allowing the algorithm the opportunity to reach a globally optimal solution.

## 2.9. Strahler order

The Strahler (or stream) ordering method was first introduced to classify river systems, but can be applied to any bifurcating system. In standard Strahler ordering, nodes at the end of a tree (in this case the arterioles) are assigned a number 1. At a bifurcation, if two vessels (segments) of the same order meet, then the order of the parent vessel is 1 higher. However, if two vessels of different orders meet,

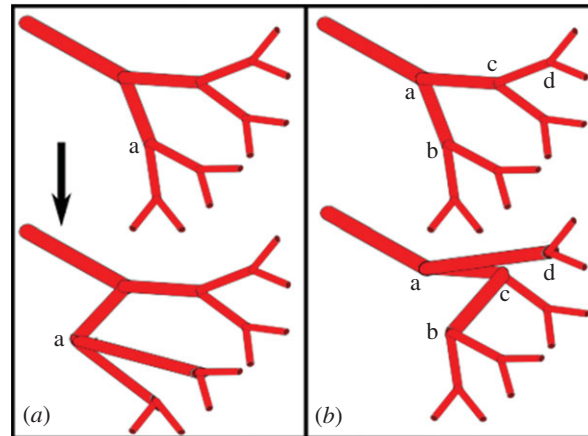


**Figure 2.** Tree modification updates.

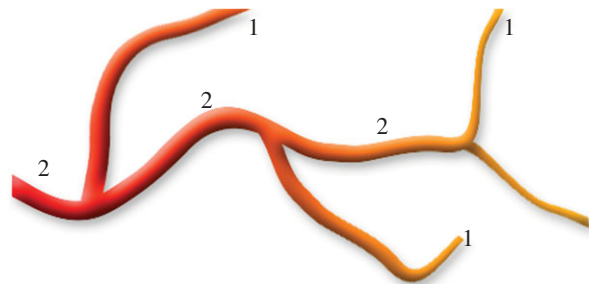


**Figure 3.** Schematic of the Strahler ordering process.

the artery supplying these vessels has the largest order of the two. For example, if two arteries of order 1 meet, then the vessel supplying these arteries has order 2. If an artery of order 3 meets an artery of order 2, then the vessel supplying these arteries has order 3 (an example is shown in figure 3). Therefore, within this scheme, vessels with the lowest order are arterioles. The major vessels have the largest order. The Strahler order used here is then diameter adjusted following the approach in [38].

Within the Strahler ordering scheme it is possible to identify continuous sections of vessels with the same order number. These are referred to as elements, so a single arterial element may pass through multiple bifurcations. Throughout this article, it is the properties of elements which will be calculated for direct comparison with [9]. We note that due to the early termination of the simulated trees, calculated order numbers are modified so that the root nodes have an order number equivalent to that of the largest arteries of real coronary arterial trees. For example, in the work of Kassab, the largest diameter defined Strahler order number is 11, corresponding to the input artery. For a computer generated tree of only 6000 nodes spanning order numbers 1–6, 5 must be added to each order number so that the orders of the root nodes (largest vessels) match and a direct comparison can be made. This is consistent with assuming that the smallest vessels in the computer generated tree correspond to vessels of order 6. Which is due to the absence of smaller vessels downstream of the smallest arteries in the *in silico* model.

### 3. Results

In this paper, globally optimized vessels are grown using an SA-based approach to supply a myocardial substrate, and validated through comparison with morphological data from the porcine arterial tree. We choose to examine the heart vasculature, as the structure of the large coronary arteries has been found to be similar between individuals [39] and the full arterial tree has been well characterized in porcine models [9]. For modelling the coronary arteries, we used the following parameters. (i) A tissue substrate representing an ellipsoidal human heart muscle of mass 218 g, constructed based on physiological parameters [40]. The right ventricle was assumed to take the form of a super ellipsoid of exponent 2.5 and the left ventricle was represented by a simple ellipsoid. Truncation of the ellipsoidal substrate was chosen



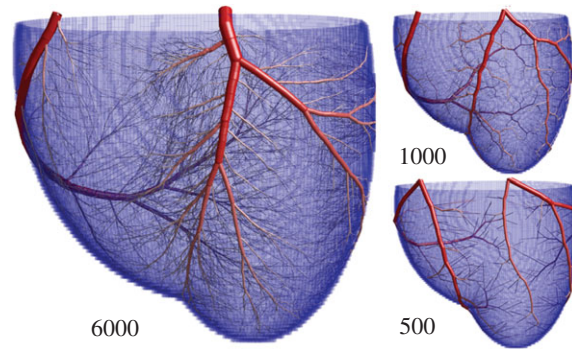


**Figure 4.** Images showing arterial trees grown with the approach detailed here. The number of terminal arterioles is increased from 500 to 6000 (the total number of arterial segments is roughly twice this). There is consistency in the positioning of the larger arteries between the numerical method and the typical arrangement of the major arteries, suggesting that the coronary arteries may be the result of a biological process seeking the global minimum in metabolic demand.

so that the mass of the tissue corresponded to a reasonable physiological value given morphological data for ventricle thickness. (ii) Blood flow through each of the terminal segments of the tree was assumed to be constant, with each arteriole supplying an equal volume of tissue and homogeneous perfusion throughout the tissue parenchyma [41]. These assumptions greatly simplify fluid dynamical calculations for estimating the total power needed to pump blood through the tree. (iii) The metabolic cost of maintaining a given volume of blood was assumed to be  $641.3 \text{ J s}^{-1}$  per metre cubed of blood [30]. For convenience, each arteriole supplies a sphere of tissue with a size calculated by assuming a mean blood flow per unit mass for cardiac muscle of  $0.8 \text{ ml min}^{-1} \text{ g}^{-1}$  [42]. The value taken from the literature was chosen such that it not only lay within the given error, but also conformed reasonably with both the ellipsoidal heart model, input flow and radii. (iv) The larger arteries with diameters greater than  $0.01 \text{ mm}$  were constrained to avoid penetration of the outer layer of heart tissue. This simplification differs slightly from real coronary vasculature, where progressive intrusion of arteries into the myocardium can be observed [43]. However, as the major arteries modelled by our method are far larger than the intra-myocardial vessels, a sharp cut-off is thought to provide a reasonable approximation. (v) The starting positions of the two root arteries were fixed with a total input flow of  $4.16 \times 10^{-6} \text{ m}^3 \text{ s}^{-1}$  [44]. Relative radii of the two inputs to the tree were constrained via  $r_1^{2.1} + r_2^{2.1} = [2.1 \text{ mm}]^{2.1}$ ; however, the relative sizes of root arteries and division of perfusion territories are determined by the method alone. (vi) The branching exponent varies throughout the coronary arterial tree, but for the larger arteries its value remains in the range 1.8–2.3. A variable branching exponent would greatly increase the computational cost of the approach, so a compromise value of 2.1 was chosen for the entire tree [45].

Coronary arterial trees containing increasing total numbers of vessels grown using the SA-based method are presented in figure 4. In real human coronary trees, there are three identifiable main coronary arteries (e.g. the schematic from [46]): left anterior descending, right cardiac artery (RCA) and left circumflex artery. The positions and relative dimensions of these are similar in most humans, with major variations observed in less than 1% of healthy individuals [47]. Trees grown using SA (figure 4) adhere well to this structure. There is a consistency in the placement of the larger arteries, although the RCA appears slightly lower, and the right marginal artery appears slightly shorter, in our models. Overall, visual inspection of the arterial structure appears extremely promising.

To provide a quantitative comparison of our trees with anatomical data, the topological characteristics of the computer generated coronary artery trees were extracted and compared with morphological data characterizing the pig coronary arteries published by Kassab *et al.* [9]. They used a combination of corrosion casting and optical sectioning to obtain detailed morphometric data, tabulated using the Strahler (or stream) ordering scheme to denote elements of the tree of varying scale. Within this scheme, the lowest Strahler order numbers correspond to the smallest arterioles and the largest numbers refer to major vessels (for details on Strahler ordering see Methods). To directly compare arterial diameters, lengths, and branching properties of our computer-generated arterial tree with real data from pig coronary arteries, averages were obtained over all elements of the same diameter defined Strahler order.

The mean vessel diameters are shown as a function of order number for a tree comprising 6000 arterioles (12000 vessel segments) in figure 5a. Excellent agreement is found between the trees generated

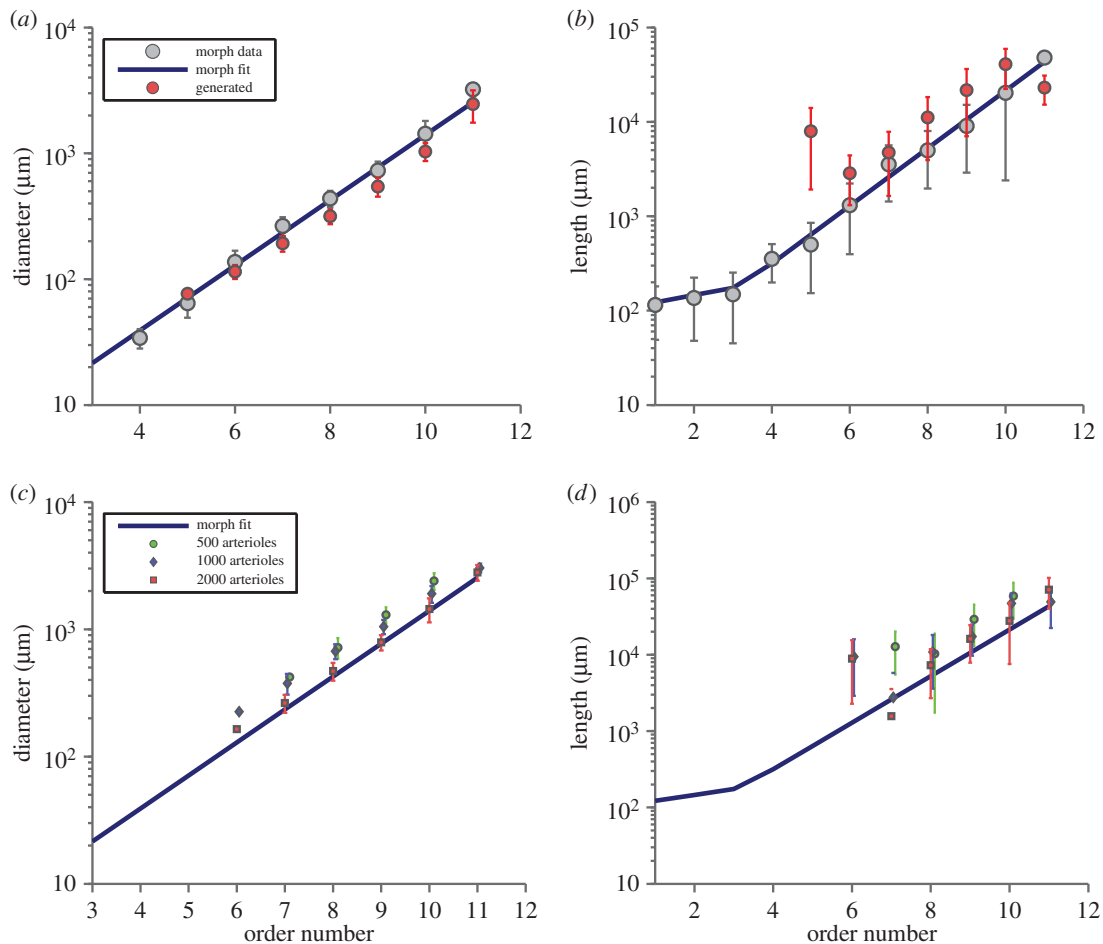


**Figure 5.** (a) Vessel diameter as a function of order in a tree with 6000 arterioles. Excellent agreement is found for vessels on all length scales. (b) Vessel length as a function of order number. Agreement is excellent for the major vessels (large order). The large variation seen for arterioles (lower order) is a result of early termination. Also shown are the morphological data reproduced from table 2 of [5] for easy comparison. (c,d) Similar to (a,b), but for smaller trees to highlight the trend towards the morphological data as tree size increases. (Error bars show standard errors, both axes are logarithmic.)

*in silico* and the morphological data. Only slight deviations from the morphological data can be seen for the smallest vessels (lowest order arteries) in the generated tree. This is likely to be due to the combination of integer order numbers and the condition that terminal sites are of constant radius. The result of this constraint is that the terminal radii will only match the anatomical data for a correct choice of the number of arterioles. Figure 5c shows the effects on diameter of increasing the number of arterioles from 500 to 2000. Agreement is generally good, regardless of the number of terminal arteries, and there is a clear trend towards matching the experimental data as simulated tree size increases. Figure 5b compares average vessel length in the model and porcine morphological data as a function of order number. For the largest arteries (high order numbers), the agreement is excellent. Although the lengths of the smaller arteries (Strahler orders  $< 7$ ) in the computer-generated tree tended to be overestimated, this can be easily explained by the fact that the smallest vessels are required to bridge a gap that would normally be filled by inclusion of lower order vessels in a larger simulation. As the number of generated vessels is increased, the agreement with morphological data improves (figure 5d).

Previously, the best methods available for the computer generation of arterial trees struggled to recreate realistic branching asymmetry. Figure 6 shows the ratio of daughter to mother vessel radii for the largest and smallest daughter vessels as a function of order number. This provides a measure of the branching asymmetry of the tree, where small ratios indicate that branching is symmetric, while ratios approaching 1 suggest a large trunk vessel with small branches. For Strahler orders corresponding to microvascular arterioles, both the computer generated and true morphology approach 0.7, which is consistent with perfectly symmetric branching where both daughter vessels are of similar size.

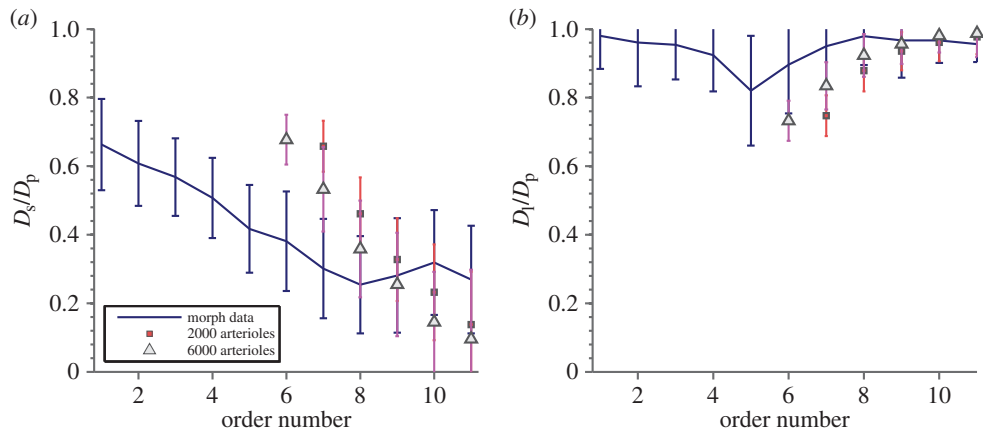


**Figure 6.** The ratio of daughter vessel diameters ( $D_s$  and  $D_l$  are the diameters of the smallest and largest daughter vessels, respectively) to diameters of parent segments  $D_p$  as a function of order number, showing how the tree tends towards more symmetric branching at lower orders. Agreement with morphological data reproduced from tables in the online supplement of [45] is good, if the early termination of the generated trees is taken into account, with the trend towards the morphological data as the tree size increases. Both graphs demonstrate that there are large trunks at high orders with the largest daughter vessel (b) of similar size to the parent vessel and another side artery which is much smaller (a). At smaller orders, the ratio becomes similar showing that the branchings of the smaller arteries are near symmetric. Realistic branching asymmetries are a clear advantage over other methods of generating arterial trees *in silico*.

Agreement with the morphological data from [45] improves as the size of the computer-generated tree increases. This is not the result of any special input parameters or initial conditions. The trees are topologically and spatially randomized before SA optimization begins, and are allowed to explore the entire parameter space during optimization. The observed asymmetry is purely the result of a balance between pumping power and metabolic maintenance cost, and is a major improvement in predicting the trunk-like structure of major vessels.

Our final figures show the effect of altering the metabolic energy cost of blood per unit volume  $m_b$ . The largest morphological change is found in the lengths of the larger arteries (figure 7). As  $m_b$  increases, bifurcation symmetry is also increased in the larger arteries and as a result there is an increase in the number of Strahler orders present in the tree (figure 7). The explanation for these scaling behaviours is evident when considering the limiting cases. For  $m_b = 0$  the power involved in pumping the blood dominates the optimization, which leads to a large, ‘snaking’ artery with small side branches that supply the tissue. This large artery would cover the entire surface of the heart, and the configuration is equivalent to a completely asymmetric binary tree. For a large  $m_b$  value (or small power cost) there is a huge penalty associated with larger arteries, and so their lengths are contracted. In order to accommodate the reduction in length, the larger arteries must bifurcate more frequently and symmetrically. Additionally, the high volume cost causes the trunk artery to minimize its total length, resulting in a much straighter path across the tissue. Less extreme examples of this behaviour can be seen in figure 8, with meandering arteries for small  $m_b$  and straight arteries for large  $m_b$ .

The change in  $m_b$  can also be interpreted as a change in length scale as follows: once the large vessels have been excluded from the tissue and all tissue is supplied, the remaining cost function that is optimized has the form

$$C = m_b \pi r^2 l + \frac{8 \mu l Q^2}{\pi r^4}.$$

Now, make the transformations  $r \rightarrow r' = Ar$ ,  $l \rightarrow l' = Al$ . Then the cost function becomes

$$C = A^3 m_b \pi r^2 l + \frac{8 \mu A l Q^2}{A^4 \pi r^4}.$$

As the optimum in the cost function is the same independent of a multiplicative factor that acts on all terms, then we can absorb a factor of  $1/A^3$  into the cost function to obtain

$$C' = A^6 m_b \pi r^2 l + \frac{8 \mu l Q^2}{\pi r^4}.$$

Identifying a new  $m'_b = A^6 m_b$  the cost function now has the same form. As changing  $m_b$  is equivalent to changing the length scale, these results suggest that there are likely to be structural differences between

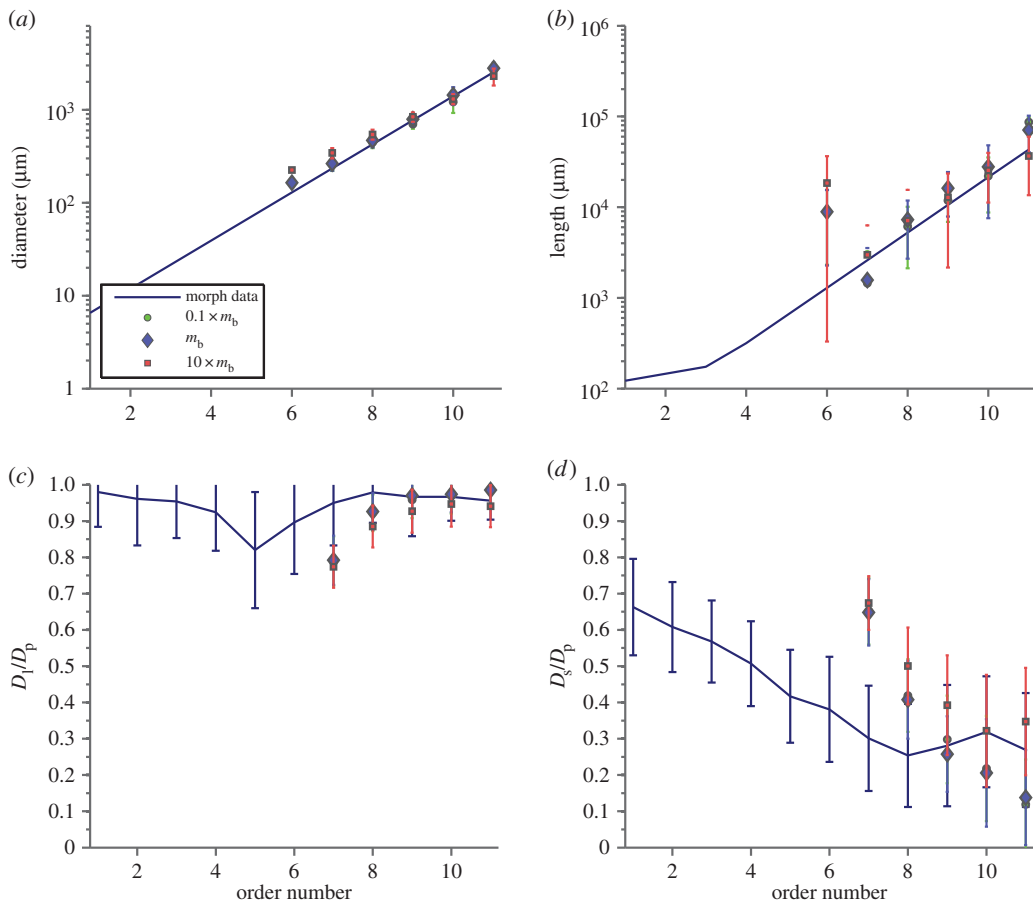


**Figure 7.** (a) Diameter as a function of order number for trees with 1000 vessels. Decreasing  $m_b$ , which describes the relative energy cost of an amount of blood and the power required to pump it, has little effect on the agreement of the diameters with morphological data. (b) For lengths however there is an obvious effect in the larger arteries, with regimes of high pumping cost being more accurate. The primary optimization for high pumping cost then is to increase the length of the largest arteries. (c,d) The main effect is a change in the asymmetry of the branching of the largest arteries—for large  $m_b$ , the branches are more symmetric than for small  $m_b$ . As  $m_b$  becomes very small, the limiting behaviour is broad trunks that wind around all the tissue, with a large number of very small offshoots that supply blood in the direct vicinity of the large vessel.

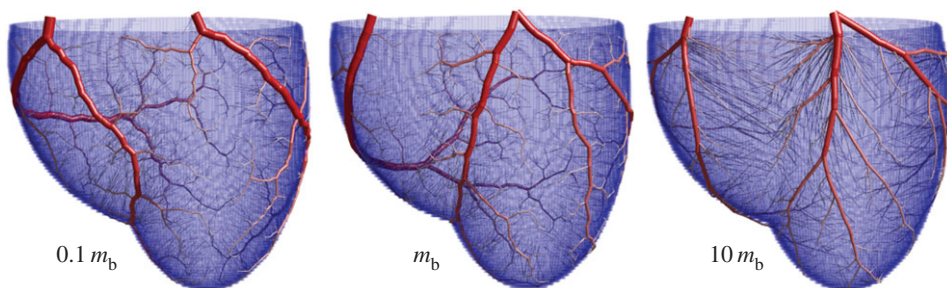


**Figure 8.** Example trees generated with different values of  $m_b$ , which changes the relative weight of the pumping power to cost of maintaining blood in the optimization. For small  $m_b$  (corresponding to small hearts), vessels in the trees wind around—this is because there is little penalty to make a single wide vessel that curves to supply blood, rather than bifurcating. For large  $m_b$  (corresponding to large hearts) the vessels travel as straight as possible.

species of different sizes, as the power required to pump blood becomes relatively more important than the metabolic demand to maintain blood volume in small vessels. In the absence of morphological data, visual comparison of the coronary arteries tentatively indicates that vessels meander around in smaller species [48] and that vessels are straighter in larger species [49].

## 4. Discussion

We have developed a powerful and universal method for growing arterial trees *in silico*, which is capable of identifying the near globally optimal configuration of arteries for arbitrarily shaped tissues with heterogeneous blood supply demands. As input, the method only needs information about the tissue structure and the entry point positions of the largest arteries. From this information, the approach generates morphologically and structurally accurate coronary arterial trees at almost every length scale. This is a significant improvement on previous optimization methods, which failed to reproduce the consistent structure found in the coronary arteries. We have shown that the method improves with the number of vessels modelled, so that, as computing power increases, there is a systematic improvement in the accuracy of the generated trees. To our knowledge, no other method can generate realistic arterial trees that closely match morphological data by taking only the shape of the tissue as input, and claim systematic improvement in the generated trees with increased computational power.

We expect that our method could have several useful applications. Our first application is to use cardiac and partial cerebral vasculature structures (e.g. MCA territory) computed using this method as input to models of embolic stroke and other infarctions, as these models require detailed vasculature structure over a range of length scales which are not available to imaging techniques [50–52]. This will require further validation of the algorithm against cerebral arterial data. Such vasculature would be downstream of the Circle of Willis, a source of major anatomical variation and probably not a structure reproducible by the current algorithm. Computational models of stroke combined with Doppler ultrasound have potential to provide further information regarding embolic burden during major operations [53].

There are several other potential applications. Models of arterial trees generated by our method may help to improve the interpretation of medical images through advanced image segmentation techniques. Vessels identified through automatic segmentation techniques can be connected via algorithms such as the one presented [54]. In addition, segmentation can be limited to the location of a reduced set of bifurcation points, and the algorithm used to fill in any missing vessels which connected them [55].

We also speculate that the algorithm could be of use in designing the structures of vasculature for artificial tissues. Once the very difficult and intricate process of making networks of vessels in artificial tissue has been achieved [56–58], the opportunity to optimize or inform their design will be available. A common problem during the growth of artificial tissue is that regions of cells can die due to lack of nutrients and oxygen. For instance, an artificial skin graft may be optimized for increased healing, by having its vasculature designed such that there is higher overall perfusion with minimal loss of useful tissue. Even more speculatively, artificially grown organs may have a vasculature designed to minimize their impact on the cardiovascular system.

**Data accessibility.** Data presented in this article can be found in a compressed zip folder as the electronic supplementary material. The folders contain Matlab scripts capable of plotting the data.

**Authors' contributions.** J.K. developed the algorithm, acquired, analysed and interpreted data, and contributed to drafting the article. E.C. co-conceived the study, co-supervised the project and contributed to drafting the article. J.P.H. conceived the study, developed initial versions of the algorithm, contributed to the analysis and interpretation of data, supervised the project and contributed to drafting of the article. All authors gave final approval for publication. **Competing interests.** We declare we have no competing interests.

**Funding.** J.K. acknowledges EPSRC grant EP/P505046/1. E.M.L.C. acknowledges support from a British Heart Foundation Intermediate Basic Science Research Fellowship (FS/10/46/28350).

**Acknowledgements.** We thank Chloe Long, Martin Bootmann and Uwe Grimm for useful discussions.

## Appendix A. Convergence and consistency

The primary purpose of the algorithm is to produce arterial tree configurations which conform to those found in living organisms. As the algorithm itself relies only upon optimization principles, the close agreement with experimental results implies an evolutionary pressure towards a structure with minimal power consumption. This is itself a far from new concept; however in this paper we have shown that energetic constraints lead not only to a morphometrically realistic tree, but also to the production of major arteries which closely follow the paths of major arteries in living systems.

Whilst it is clear that the algorithm produces both morphometrically and geometrically realistic structures, what is not clear is how close the optimization procedure gets to the global energy minimum, or indeed whether there is a non-degenerate energy minimum at all. For any given topological configuration there is a single, non-degenerate energy minimum which it is possible to approach using



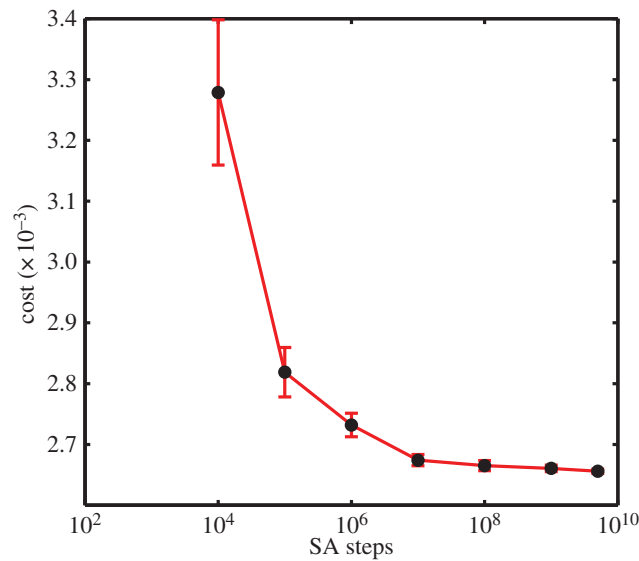


**Figure 9.** Average cost and standard error versus SA steps for a 127 node tree grown in a two-dimensional plane.

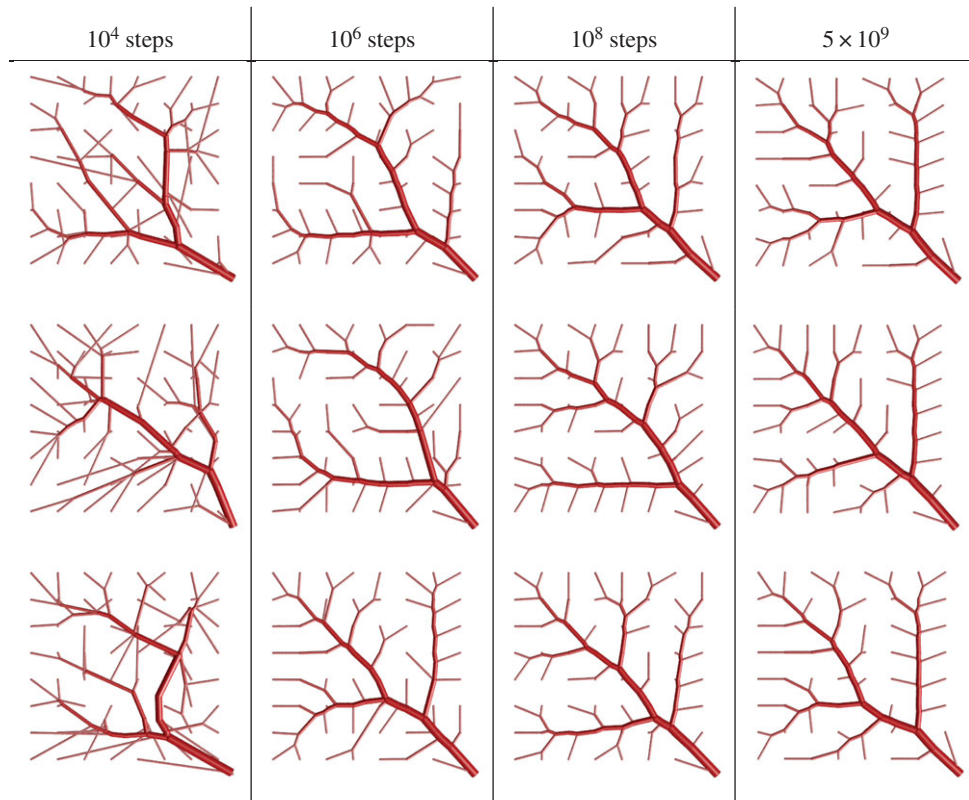


**Figure 10.** Example of trees grown for various different numbers of SA step numbers.

Newton–Raphson (provided the solution space is convex, which would not be true for more complex structures). By contrast, the topological space for any even modestly sized tree is huge, highly degenerate and not easily searchable. Even if one excludes degenerate topological structures, which in the case of the swap node procedure outlined earlier would imply never swapping two nodes with the same number of distal terminal sites, the number of possible configurations is still massive. It is entirely possible that two distinct topological configurations share a degenerate energy level, and proving that this is not the case appears difficult.



While it may be that the global energy minimum is highly degenerate, the algorithm itself can still be characterized in terms of reliability and convergence. For reliability, we can perform visual inspections on trees and assess their similarity. It must be noted here that the geometry in which the tree is grown will have a large effect on the consistency of the results. For instance, in the case of a circular section of tissue with an input in the centre, there is a high degree of rotational symmetry. In the case of convergence, we can produce many trees and plot the frequency distribution of their resultant energies, or as in this case the average and variance of the cost as a function of SA steps.

The convergence and consistency test trees were generated on a two-dimensional plane with the input placed in one corner. The trees consisted of 127 nodes total (64 end nodes) and had a bifurcation exponent of 3.0. The two-dimensional tissue plane was sized at 10 cm by 10 cm and the root radius at 2.4 mm. Each tree was optimized for a given number of SA steps, with the minimum energy of the SA run being recorded. The average energy reached for a given number of SA steps was then calculated (figure 9). The results show a clear trend towards lower average energy and standard deviation as the number of SA steps increases. The high variance at the lower numbers of SA steps is typical of a system which has been quenched, i.e. high temperature disorder has been locked into the system, which had not had sufficient time to reach equilibrium.

For the consistency test we have produced figure 10, which shows trees generated for three different numbers of steps. As would be expected, at low numbers of SA steps the trees are very dissimilar; however as the number of steps increases the similarity between the overall trees increases dramatically, with a main diagonal artery dominating the structure.

## References

- Zamir M. 2000 *The physics of pulsatile flow*. Berlin, Germany: Springer.
- Frame MDS, Sarelius IH. 1995 Energy optimization and bifurcation angles in the microcirculation. *Microvasc. Res.* **50**, 301–310. (doi:10.1006/mvres.1995.1060)
- Murray CD. 1926 The physiological principle of minimum work. I. The vascular system and the cost of blood volume. *Proc. Natl Acad. Sci. USA* **12**, 207–214. (doi:10.1073/pnas.12.3.207)
- Rossitti S, Löfgren J. 1993 Vascular dimensions of the cerebral arteries follow the principle of minimum work. *Stroke* **24**, 371–377. (doi:10.1161/01.STR.24.3.371)
- Kassab GS, Rider CA, Tang NJ, Fung YC. 1993 Morphometry of pig coronary arterial trees. *Am. J. Physiol.* **265**, H350–H365.
- Cassot F, Lauwers F, Lorthois S, Puwanarajah P, Cances-Lauwers V, Duvernoy H. 2010 Branching patterns for arterioles and venules of the human cerebral cortex. *Brain Res.* **1313**, 62–78. (doi:10.1016/j.brainres.2009.12.007)
- Huo Y, Kassab GS. 2012 Intraspinal scaling laws of vascular trees. *Biomed. Eng.* **9**, 190–200. (doi:10.1098/rsif.2011.0270)
- Huo Y, Kassab GS. 2009 A scaling law of vascular volume. *Biophys. J.* **96**, 347–353. (doi:10.1016/j.bpj.2008.09.039)
- Kassab GS. 2006 Scaling laws of vascular trees: of form and function. *Am. J. Physiol. Heart Circ. Physiol.* **290**, H894–H903.
- Bengtsson HU, Edén P. 2003 A simple model for the arterial system. *J. Theor. Biol.* **221**, 437–443. (doi:10.1006/jtbi.2003.3198)
- West GB, Brown JH, Enquist BJ. 1997 A general model for the origin of allometric scaling laws in biology. *Science* **276**, 122–126. (doi:10.1126/science.276.5309.122)
- Karch R, Neumann F, Neumann M, Schreiner W. 1999 A three-dimensional model for arterial tree representation, generated by constrained constructive optimization. *Comput. Biol. Med.* **29**, 19–38. (doi:10.1016/S0010-4825(98)00045-6)
- Karch R, Neumann F, Neumann M, Schreiner W. 2000 Staged growth of optimized arterial model trees. *Ann. Biomed. Eng.* **28**, 495–511. (doi:10.1114/1.1290)
- Kaimovitz B, Lanir Y, Kassab GS. 2005 Large-scale 3-D geometric reconstruction of the porcine coronary arterial vasculature based on detailed anatomical data. *Ann. Biomed. Eng.* **33**, 1517–1535. (doi:10.1007/s10439-005-7544-3)
- Schreiner W, Buxbaum PF. 1993 Computer optimization of vascular trees. *IEEE Trans. Biomed. Eng.* **40**, 482–491. (doi:10.1109/10.243413)
- Kaimovitz B, Lanir Y, Kassab GS. 2010 A full 3-D reconstruction of the entire porcine coronary vasculature. *Am. J. Phys. Heart Circ. Phys.* **299**, 1064–1067. (doi:10.1152/ajpheart.00151.2010)
- Mayrovitz HN, Roy J. 1983 Microvascular blood flow: evidence indicating a cubic dependence on arteriolar diameter. *Am. J. Physiol.* **245**, H1031–H1038.
- Horsfield K, Wolstenberg MJ. 1989 Diameter and cross-sectional areas of branches in the human pulmonary arterial tree. *Anat. Rec.* **223**, 245–251. (doi:10.1002/ar.1092230302)
- Karch R, Neumann F, Neumann M, Schreiner W. 2000 Staged growth of optimized arterial model trees. *Ann. Biomed. Eng.* **28**, 495–511. (doi:10.1114/1.1290)
- Schreiner W, Neumann F, Neumann M, Karch R, End A, Roedler SM. 1997 Limited bifurcation asymmetry in coronary arterial tree models generated by constrained constructive optimization. *J. Gen. Physiol.* **109**, 129–140. (doi:10.1085/jgp.109.2.129)
- Schreiner W, Karch R, Neumann M, Neumann F, Szawlowski P, Roedler S. 2006 Optimized arterial trees supplying hollow organs. *Med. Eng. Phys.* **28**, 416–429. (doi:10.1016/j.medengphys.2005.07.019)
- Hahn H, Georg M, Peitgen H-O. 2005 Fractal aspects of three-dimensional vascular constructive optimization. In *Fractals in biology and medicine* (eds GA Losa, D Merlini, TF Nonnenmacher, ER Weibel). Mathematics and Biosciences in Interaction, pp. 55–66. Basel, Switzerland: Birkhäuser.
- Kassab GS, Pallancae E, Schatz A, Fung YC. 1997 Longitudinal position matrix of the pig coronary vasculature and its hemodynamic implications. *Am. J. Physiol.* **273**, H2832–H2842.
- Fung GSK, PaulSegars W, Gullberg GT, Tsui BMW. 2011 Development of a model of the coronary arterial tree for the 4d xcat phantom. *Phys. Med. Biol.* **56**, 5651–5663. (doi:10.1088/0031-9155/56/17/012)
- Perfahl H et al. 2011 Multiscale modelling of vascular tumour growth in 3D: the roles of domain size and boundary conditions. *PLoS ONE* **6**, e14790. (doi:10.1371/journal.pone.0014790)
- Anderson ARA, Chaplain MAJ. 1998 Continuous and discrete mathematical models of tumor-induced angiogenesis. *Bull. Math. Biol.* **60**, 857–899. (doi:10.1006/bulm.1998.0042)
- McDougall SR, Anderson ARA, Chaplain MAJ. 2006 Mathematical modelling of dynamic adaptive tumour-induced angiogenesis: clinical implications and therapeutic targeting strategies. *J. Theor. Biol.* **241**, 564–589. (doi:10.1016/j.jtbi.2005.12.022)
- Das A, Lauffenburger D, Asada H, Kamm RD. 2010 A hybrid continuum–discrete modelling approach to predict and control angiogenesis: analysis of combinatorial growth factor and matrix effects on vessel-sprouting morphology. *Phil. Trans. R. Soc. A* **368**, 2937–2960. (doi:10.1098/rsta.2010.0085)
- Kirkpatrick S, Gelatt CD, Vecchi MP. 1983 Optimization by simulated annealing. *Science* **220**, 671–680. (doi:10.1126/science.220.4598.671)
- Liu Y, Kassab GS. 2007 Vascular metabolic dissipation in Murray's law. *Am. J. Physiol. Heart Circ. Physiol.* **292**, H1336–H1339. (doi:10.1152/ajpheart.00906.2006)

31. Vinnakota KC, Bassingthwaite JB. 2004 Myocardial density and composition: a basis for calculating intracellular metabolite concentrations. *Am. J. Physiol. Heart Circ. Physiol.* **286**, H1742–H1749. (doi:10.1152/ajpheart.00478.2003)
32. Uren NG, Melin JA, De Bruyne B, Wijns W, Baudhuin T, Camici PG. 1994 Relation between myocardial blood flow and the severity of coronary-artery stenosis. *New Engl. J. Med.* **330**, 1782–1788. (doi:10.1056/NEJM199406233302503)
33. Hall JE. 2010 *Guyton and Hall textbook of medical physiology*. Amsterdam, The Netherlands: Elsevier.
34. King RB, Bassingthwaite JB. 1989 Temporal fluctuations in regional myocardial flows. *Pflügers Arch.* **413**, 336–342. (doi:10.1007/BF00584480)
35. Amanatides J, Woo A. 1987 A fast voxel traversal algorithm for ray tracing. *Eurographics* **87**, 3–10.
36. Henderson D, Jacobson SH, Johnson AW. 2003 The theory and practice of simulated annealing. In *Handbook of metaheuristics* (eds F Glover, GA Kochenberger). International Series in Operations Research & Management Science, vol. 57, pp. 287–319. New York, NY: Kluwer. (doi:10.1007/0-306-48056-5\_10)
37. Kirkpatrick S, Gelatt CD, Vecchi MP. 1983 Optimization by simulated annealing. *Science* **220**, 671–680. (doi:10.1126/science.220.4598.671)
38. Jiang ZL, Kassab GS, Fung YC. 1994 Diameter-defined Strahler system and connectivity matrix of the pulmonary arterial tree. *J. Appl. Physiol.* **76**, 882–892.
39. Glenny R, Bernard S, Neradilek B, Polissar N. 2007 Quantifying the genetic influence on mammalian vascular tree structure. *Proc. Natl Acad. Sci. USA* **104**, 6858–6863. (doi:10.1073/pnas.0610954104)
40. Van Den Broek JJM, Van Den Broek MHL. 1980 Application of an ellipsoidal heart model in studying left ventricular contractions. *J. Biomech.* **13**, 493–503. (doi:10.1016/0021-9290(80)90342-5)
41. Pries AR, Secomb TW. 2009 Origins of heterogeneity in tissue perfusion and metabolism. *Cardiovasc. Res.* **81**, 328–335. (doi:10.1093/cvr/cvn318)
42. Klocke FJ, Bunnell IL, Greene DG, Wittenberg SM, Visco JP. 1974 Average coronary blood flow per unit weight of left ventricle in patients with and without coronary artery disease. *Circulation* **50**, 547–559. (doi:10.1161/01.CIR.50.3.547)
43. Sunni S, Bishop SP, Kent SP, Geer JC. 1986 Diabetic cardiomyopathy. A morphological study of intramyocardial arteries. *Arch. Pathol. Lab. Med.* **110**, 375–381.
44. Johnson K, Sharma P, Oshinski J. 2008 Coronary artery flow measurement using navigator echo gated phase contrast magnetic resonance velocity mapping at 3.0 T. *J. Biomech.* **41**, 595–602. (doi:10.1016/j.jbiomech.2007.10.010)
45. Kaimovitz B, Huo Y, Lanir Y, Kassab GS. 2008 Diameter asymmetry of porcine coronary arterial trees: structural and functional implications. *Am. J. Physiol. Heart Circ. Physiol.* **294**, H714–H723. (doi:10.1152/ajpheart.00818.2007)
46. OpenStax College. 2013 Anatomy and physiology. See <http://cnx.org/content/col11496/1.6/>.
47. Gharib AM, Ho VB, Rosing DR, Herzka DA, Stuber M, Arai AE, Pettigrew RI. 2008 Coronary artery anomalies and variants: technical feasibility of assessment with coronary MR angiography at 3 T. *Radiology* **247**, 220–227. (doi:10.1148/radiol.2471070274)
48. Yoldas A, Ozmen E, Ozdemir V. 2010 Macroscopic description of the coronary arteries in Swiss albino mice (*Mus musculus*). *J. S. Afr. Vet. Assoc.* **81**, 247–252. (doi:10.4102/jsava.v81i4.156)
49. Ozgel O, Haligur A, Dursun N, Karakurum E. 2004 The macroanatomy of coronary arteries in donkeys (*Equus asinus* L.). *Anat. Histol. Embryol.* **33**, 278–283. (doi:10.1111/j.1439-0264.2004.00548.x)
50. Chung EML, Hague JP, Evans DH. 2007 Revealing the mechanisms underlying embolic stroke using computational modelling. *Phys. Med. Biol.* **52**, 7153–7166. (doi:10.1088/0031-9155/52/23/025)
51. Hague JP, Chung EML. 2009 Statistical physics of cerebral embolization leading to stroke. *Phys. Rev. E* **80**, 051912. (doi:10.1103/PhysRevE.80.051912)
52. Hague JP, Banahan C, Chung EML. 2013 Modelling of impaired cerebral blood flow due to gaseous emboli. *Phys. Med. Biol.* **58**, 4381. (doi:10.1088/0031-9155/58/13/4381)
53. Chung EML *et al.* 2015 Size distribution of air bubbles entering the brain during cardiac surgery. *PLoS ONE* **10**, e0122166. (doi:10.1371/journal.pone.0122166)
54. Jiang Y, Zhuang Z, Sinusas AJ, Papademetris X. 2010 Vascular tree reconstruction by minimizing a physiological functional cost. In *IEEE Computer Society Conf. on Computer Vision and Pattern Recognition Workshops*, pp. 178–185. (doi:10.1109/CVPRW.2010.5543593)
55. Bruyninckx P, Loeckx D, Vandermeulen D, Suetens P. 2010 Segmentation of liver portal veins by global optimization. *Proc. SPIE* **7624**, 76241Z. (doi:10.1117/12.843995)
56. Novosel EC, Kleinhans C, Kluger PJ. 2011 Vascularization is the key challenge in tissue engineering. *Adv. Drug Deliv. Rev.* **63**, 300–311. (doi:10.1016/j.addr.2011.03.004)
57. Kim S, Lee H, Chung M, Jeon NL. 2013 Engineering of functional, perfusable 3D microvascular networks on a chip. *Lab. Chip* **13**, 1489–1500. (doi:10.1039/c3lc41320a)
58. Baranski JD *et al.* 2013 Geometric control of vascular networks to enhance engineered tissue integration and function. *Proc. Natl Acad. Sci. USA* **110**, 7586–7591. (doi:10.1073/pnas.1217796110)